Rare-earth (RE) nanolaminates Mo$_4$RE$_4$Al$_7$C$_3$ featuring ferromagnetism and mixed-valence states

Q. Tao,[1] T. Ouisse,[2] D. Pinek,[2] O. Chaix-Pluchery,[2] F. Wilhelm,[3] A. Rogalev,[3] C. Opagiste,[4] L. Jouffret,[5] A. Champagne,[6] J.-C. Charlier,[6] J. Lu,[1] L. Hultman,[1] M. W. Barsoum,[7] and J. Rosen[1]

[1]*Thin Film Physics, Department of Physics, Chemistry and Biology (IFM), Linköping University, SE-581 83 Linköping, Sweden*
[2]*Université Grenoble-Alpes, CNRS, Grenoble INP, LMGP, F-38000 Grenoble, France*
[3]*European Synchrotron Radiation Facility (ESRF), CS40220, F-38043 Grenoble Cedex 9, France*
[4]*Université Grenoble-Alpes, CNRS, Institut NEEL, Grenoble INP, F-38000 Grenoble, France*
[5]*Institut de Chimie de Clermont Ferrand, F-63178 Aubière, France*
[6]*Institute of Condensed Matter and Nanosciences, UCLouvain, B-1348 Louvain-la-Neuve, Belgium*
[7]*Department of Materials Science and Engineering, Drexel University, Philadelphia, Pennsylvania 19104, USA*

Rare-earth-based (RE) nanolaminates have attracted attention recently because of their complicated magnetism and their potential as precursors for strongly correlated two-dimensional materials. In this work, we synthesized a class of nanolaminates with a Mo$_4$RE$_4$Al$_7$C$_3$ chemistry, where RE = Ce or Pr. Powder samples of both phases were characterized with respect to structure and composition. Single crystals of Mo$_4$Ce$_4$Al$_7$C$_3$ were used for magnetization measurements. The crystal structure was investigated by means of x-ray diffraction and scanning transmission electron microscopy. Magnetization analysis reveals a ferromagnetic ground state with a Curie temperature of ∼10.5 K. X-ray absorption near-edge structure provides experimental evidence that Ce is in a mixed-valence state. X-ray magnetic circular dichroism shows that only the Ce atoms with $4f^1$ configuration occupying one of the two possible sites are ferromagnetically coupled, with a saturation moment of ∼1.2 μ_B per atom. We thus classify Mo$_4$Ce$_4$Al$_7$C$_3$ as a ferromagnetic, mixed-valence compound.

I. INTRODUCTION

Rare-earth (RE) compounds exhibit a variety of magnetic and electronic ground states through the hybridization between $4f$ and conduction electrons [1–3]. Heavy fermion compounds, primarily those containing Ce and Yb, are prototype systems for the study of quantum critical [4] and collective quantum states [5]. In addition to the orbital and valence degrees of freedom generating a multitude of ground states [6], the discovery of new layered RE compounds that can act as precursors for the synthesis of two-dimensional (2D) magnetic materials is another fruitful avenue. In the latter domain, it has recently been shown that RE intercalation in graphene grown on Si-face SiC substrates can lead to substantial doping of the graphene layers and quite high 2D electron densities [7]. However, transferring large-scale and mono- or multilayers while preserving the integrity of the RE dopants and maintaining regular order constitutes a real challenge. An alternative strategy is to use 2D systems, for which high metallic carrier densities are an intrinsic material property, and to incorporate the RE element as a regular, ordered member of the original lattice in order to optimize compound stability and robustness. A first step toward this goal is to synthesize three dimensional (3D) layered compounds, which can be exfoliated to form magnetic 2D systems, in which the RE's magnetism is potentially transferred to the itinerant electrons and used for electron spin control and/or injection. Before proceeding further, we note that in 2011 it was shown that it is relatively straightforward to selectively

etch individual atomic layers (mostly Al) from the laminated ternary 3D carbides (MAX phases; see below) for conversion into their 2D metal carbide (MXene) counterparts [8].

In the present paper, we report on the synthesis of a family of magnetically ordered nanolaminates with a Mo$_4$RE$_4$Al$_7$C$_3$ chemistry. This discovery was made while exploring the so called i-MAX phases. The M$_{n+1}$AX$_n$ (MAX) phases, where M is an early transition metal, A is an A-group element (mostly groups 13 and 14), X is C and/or N, and $n = 1 - 3$, are machinable metallic carbides/nitrides with a nanolamellar structure [9]. In 2017, in-plane ordered or i-MAX phases were reported [10,11]. In these quaternary compounds where $n = 1$, viz. (M$^1_{2/3}$, M$^2_{1/3}$)$_2$AlC, the M^1 and M^2 transition metals are ordered in the M basal plane. When the latter are etched they form i-MXenes [10,12]. The unique feature of the i-MAX phases is the possibility to derive i-MXenes with ordered vacancies *or* M element order, from the same parent material, through etching of both Al and M^2 or Al only, respectively [13]. The first i-MAX phase discovered was (Mo$_{2/3}$, Sc$_{1/3}$)$_2$AlC [10]. The fact that Sc could be incorporated in an i-MAX phase led us to try other RE elements. Indeed, we recently synthesized 11 new RE i-MAX phases (Ref. [14]).

During the synthesis of the aforementioned RE i-MAX phases, we discovered a family of RE-based nanolaminates with a chemical formula of Mo$_4$RE$_4$Al$_7$C$_3$—henceforth referred to as the 4473 phases—where RE = Ce or Pr. These phases, though of a different composition compared to the i-MAX phases, display the same characteristic in-plane chem-

ical order of the Mo and RE elements. Not only did we synthesize these materials in powder form, but we also grew relatively large single crystals that, in turn, allowed us to carry out a comprehensive materials characterization, more focused on $Mo_4Ce_4Al_7C_3$. Calculated Raman-active vibrational modes for this phase were found to be in very good agreement with the measured Raman spectra. Based on magnetization measurements, x-ray absorption near-edge structure (XANES), and x-ray magnetic circular dichroism (XMCD), we find a ferromagnetic response and that at least one of the two inequivalent Ce atomic sites is in a mixed valence state.

II. EXPERIMENT

A. Materials synthesis

1. Powder sample preparation

Powder samples were synthesized at Linköping University (LiU). The starting powders were graphite (99.999%), Mo (99.99%) (Sigma-Aldrich), Al (99.8% Alfa Aesar), Ce (99.9%), and Pr (99.9%) (Stanford Advanced Material). Stoichiometric amounts of the elements were mixed in an agate mortar, heated to 1500 °C in an alumina crucible under flowing argon, and held at that temperature for 5 h. After furnace cooling down to room temperature, the slightly sintered body was crushed manually to obtain fine powders for x-ray diffraction (XRD) and scanning transmission electron microscopy (STEM).

2. Single-crystal growth

Single-crystalline platelets of $Mo_4Ce_4Al_7C_3$—with areas up to a few mm^2—were grown at the LMGP in Grenoble using a high-temperature solution growth process that is quite similar to that already described in Refs. [15,16] for growing MAX phase single crystals. In short, Mo, Ce, and Al are melted in a sealed graphite crucible at 1800 °C in an induction-heated reactor. A soak time of a few hours is used to allow the Mo to melt and the C—from the crucible walls—to dissolve in the melt solution. After soaking, the temperature is reduced to 1500 °C in 0.5 h, and a linear cooling ramp of a few days, down to 800 °C, is used to nucleate and grow the crystals near the molten flux surface that is the coolest point.

Since only the binary phase diagrams are known for the present materials system, the solution composition was chosen by systematically avoiding compositions lying close to any of the existing stable binary compounds. A starting favorable, and typical, Mo:Ce:Al atomic composition is 0.1:0.45:0.45. The crystals are separated from the solidified flux by simply placing the latter for one to two days in a fume hood at room temperature (RT). The oxidation of the excess RE transforms the flux into a yellow powder, leaving behind flux-free single crystals. Due to the structure anisotropy and the lack of screw dislocations, the silver-colored shiny platelets exhibit high aspect ratios. The largest platelet areas were around 3 mm^2. The average crystals were $\approx 100\,\mu m$ thick. Atomic force microscope images (not shown) suggest that the growth proceeds through a step flow mechanism resulting in regular terraces separated by steps with a height that is, most of the time, equal to one unit cell.

B. Materials characterization and computational details

1. X-ray diffraction

XRD (θ-2θ scans) on the powder samples were performed using a PANalytical X'Pert powder diffractometer, with a Cu source ($\lambda = 1.54$ Å). The optics utilized for these measurements were a graded Bragg-Brentano HD with ½° divergent and ½° antiscattering slits for the incident beam side, and a 5 mm antiscattering slit together with a Soller slit for the diffracted beam side. A $5° - 90°$ continuous scan was performed on the sample using a step size of 0.016° with a 10 s time per step.

A metallic $Mo_4Ce_4Al_7C_3$ single-crystal approximately $0.029 \times 0.174 \times 0.333\,mm^3$ in size was used at Institut de Chimie de Clermont-Ferrand (ICCF) for the measurement of x-ray intensity data for structural determination on a Bruker APEX2 SC-diffractometer (Appendix A). Determination of the final cell constants is based upon the refinement of the XYZ-centroids of reflections above $20\,\sigma(I)$. Data were corrected for absorption effects using the Numerical Mu from formula method (SADABS). The structure was solved and refined at ICCF using the Bruker SHELXTL Software Package [17]. A total of five different single crystals were examined, and all gave the same structure.

2. Scanning transmission electron microscopy

STEM combined with high-angle annular dark-field imaging and selected area electron diffraction (SAED) were performed in the double-corrected Linköping FEI Titan^{3}60 − 300 operated at 300 kV. The specimens, both powder and single-crystal were prepared by embedding ground powder in a Cu grid with carbon film.

3. Vibrational properties: Raman scattering and computational details

Single-crystal Raman spectra were recorded at LMGP using a Horiba/Jobin Yvon LabRam spectrometer equipped with a liquid-nitrogen-cooled charge-coupled device detector. The measurements were carried out in the micro-Raman mode at RT. The 514.5 nm exciting line of an Ar^+ laser was focused to a spot size of $\sim 1\,\mu m$ on the sample surface with an incident power of 0.7 mW. Raman spectra were calibrated using a silicon reference spectrum.

The vibrational properties of $Mo_4Ce_4Al_7C_3$ were calculated using the ABINIT package [18], which is based on plane-wave basis sets to represent the electronic wave functions and charge densities. *Ab initio* calculations were performed using the generalized-gradient approximation (GGA) for the exchange-correlation functional as proposed by Perdew, Burke, and Ernzerhof (PBE) [19]. Optimized norm-conserving Vanderbilt pseudopotentials (ONCVPSP-PBE) [20] were used to describe core-valence interaction. Configurations of $C-2s^22p^2$, $Al-3s^23p^1$, $Mo-4s^24p^64d^{10}5s^1$, and $Ce-5s^25p^65d^16s^2$ were treated as valence electrons, and the compound was treated as nonmagnetic (no magnetic moments were included in the calculations). A plane-wave basis set, with a converged energy cutoff 80 Ry, was used to represent the wave functions. The first Brillouin zone was sampled with a $12 \times 12 \times 12$ Monkhorst-Pack k-point grid. Starting with the experimental lattice parameters, the atomic positions
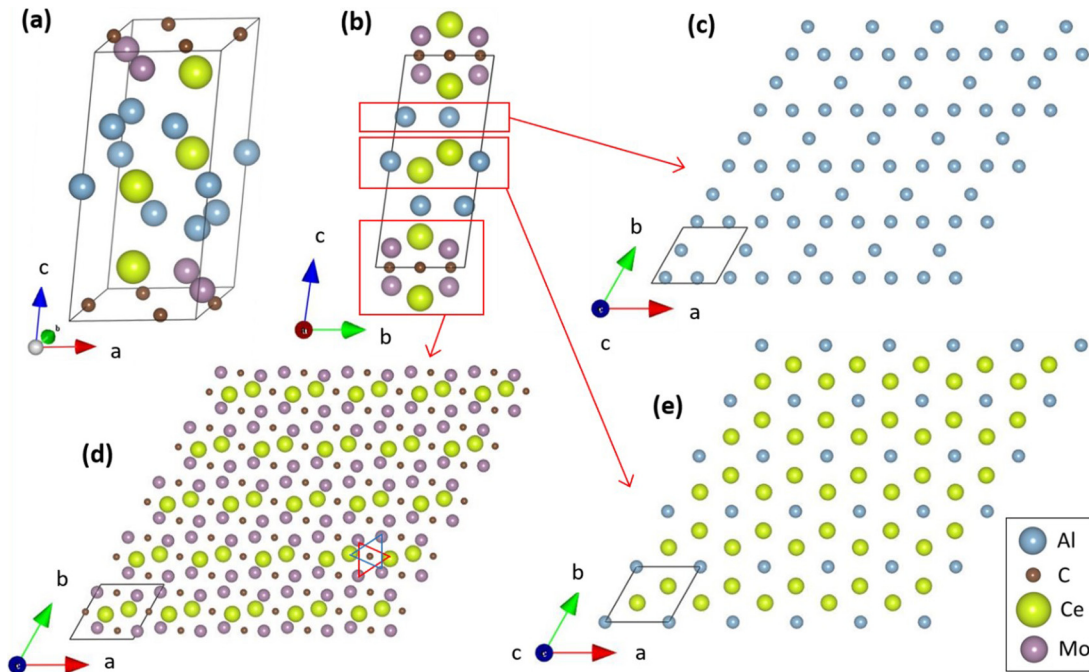
FIG. 1. (a) Unit cell of Mo$_4$Ce$_4$Al$_7$C$_3$, and (b) the crystal along the [100] zone axis. (c) Top view of the Al plane after projection along [001], showing kagomé-like ordering. (d) Top view of the Ce-Mo-C-Mo-Ce planes after projection along [001]. (e) Top view of the Ce-Mo planes after projection along [001]. In (d), the red and blue triangles define a C-centered octahedron comprised of Mo and Ce atoms.

were fully optimized until the largest force was smaller than 2.5×10^{-4} eV/Å.

4. Magnetization measurements

We used a commercial Quantum Design MPMS magnetometer for measurements in magnetic fields, H, up to 9 T. Quantitative magnetization measurements were performed on a 0.36 mg single crystal in the 2–300 K temperature range. Temperature ramps were achieved both in the field-cooled (FC) and zero-field-cooled (ZFC) modes. Isothermal magnetization curves M(H) were measured up to 300 K. In the paramagnetic regime, the inverse of the magnetic susceptibility was deduced from Arrott-type plots, viz. plots of M^2 versus H/M.

5. X-ray absorption near-edge structure and
x-ray magnetic circular dichroism

X-ray absorption near-edge structure (XANES) and x-ray magnetic circular dichroism (XMCD) spectra, at the Ce $L_{3,2}$ and Mo $L_{3,2}$ edges, were made at the European Synchrotron Radiation Facility (ESRF) beamline ID12 [21]. The source of the x rays was a helical undulator either of Apple-II type for the Ce L edges or HELIOS-II type for the Mo L edges. The XANES spectra were recorded on a mm-sized single crystal using the total fluorescence yield detection mode. For the XMCD measurements, a magnetic field of 1 T was applied collinear to the incoming x-ray beam and perpendicular to the sample surface, i.e., along the c axis. The XMCD signal was obtained as a direct difference of the XANES spectra recorded with right and left circularly polarized x rays. The sample was cooled down to 2.1 K. To ensure that the XMCD spectra were free from any experimental artifacts, the data were collected

for both directions of the applied magnetic field, parallel and antiparallel to the x-ray beam. The degree of circular polarization of the monochromatic x-ray beam at the Ce L edges was estimated to be ∼85%, whereas at the Mo L_3 and L_2 edges they were only ∼13% and ∼5%, respectively. The x-ray absorption spectra for right and left circularly polarized x-ray beams, for both Ce and Mo, were then corrected individually for self-absorption effects, and the spectra at the L_3 edge were normalized to unity, whereas the spectra at the L_2 edge were normalized to one-half, respecting, therefore, the statistical ratio of 2/1. Finally, the XMCD spectra were corrected for the rate of circular polarization.

III. RESULTS AND DISCUSSION

A. Crystal structure

The crystal structure of Mo$_4$Ce$_4$Al$_7$C$_3$—obtained from analysis of the single-crystal XRD results—was found to be triclinic (space group 2, P-1) with one formula unit per unit cell [Fig. 1(a)]. The nonequivalent atomic positions are distributed in special Wyckoff positions $2i$ (two Ce, two Mo, three Al, and one C atom), $1c$ (one C atom), and $1b$ (one Al atom). The final cell parameters resulting from the structural refinement are as follows: $a = 5.5517(5)$ Å, $b = 5.5797(5)$ Å, $c = 11.6848(10)$ Å, $\alpha = 81.157(4)°$, $\beta = 85.827(4)°$, and $\gamma = 60.250(4)°$. The unit-cell volume is $310.51(5)$ Å^3. The whole structural parameters related to the triclinic phase are given in Table I. Details concerning the structural determination from the single-crystal XRD results are given in Appendix A.

TABLE I. Structural parameters obtained from structure refinement of $Mo_4Ce_4Al_7C_3$ single-crystal XRD results.

Chemical formula	$Mo_4Ce_4Al_7C_3$	
Formula weight	1169.13 g/mol	
Temperature	173(2) K	
Wavelength	0.71073 Å	
Crystal size	$0.029 \times 0.174 \times 0.333$ mm	
Crystal system	triclinic	
Space group	$2\ (P-1)$	
Unit-cell dimensions	$a = 5.5517(5)$ Å	$\alpha = 81.157(4)°$
	$b = 5.5797(5)$ Å	$\beta = 85.827(4)°$
	$c = 11.6848(10)$ Å	$\gamma = 60.250(4)°$
Volume	$310.51(5)$ Å^3	
Z	1	
Mo	$2i$ (0.670, 0.793, 0.087)	$2i$ (0.991, 0.143, 0.092)
Ce	$2i$ (0.339, 0.453, 0.145)	$2i$ (0.333, 0.349, 0.458)
Al	$2i$ (0.834, 0.898, 0.290)	$2i$ (0.831, 0.407, 0.291)
	$2i$ (0.337, 0.904, 0.290)	$1b$ (0.000, 0.000, 0.500)
C	$2i$ (0.674, 0.155, 0.000)	$1c$ (0.000, 0.500, 0.000)
Density (calculated)	6.252 g/cm^3	
Absorption coefficient	18.691 mm^{-1}	
$F(000)$	509	

Figure 2 shows STEM images of the $Mo_4Ce_4Al_7C_3$ along the [110] and [$\bar{1}$00] zone axes, along with SAED patterns, obtained from a single-crystal sample. In these micrographs, the Ce atoms appear brightest due to Z contrast; Mo and Al are less bright, and the lightest, C, is invisible. The crystal structure consists of a $(Mo_{2/3}Ce_{1/3})_2C$ layer and three Al-Ce layers. The $(Mo_{2/3}Ce_{1/3})_2C$ layer is basically the same as in the *i*-MAX phases, viz. the $(Mo_{2/3}Sc_{1/3})_2C$
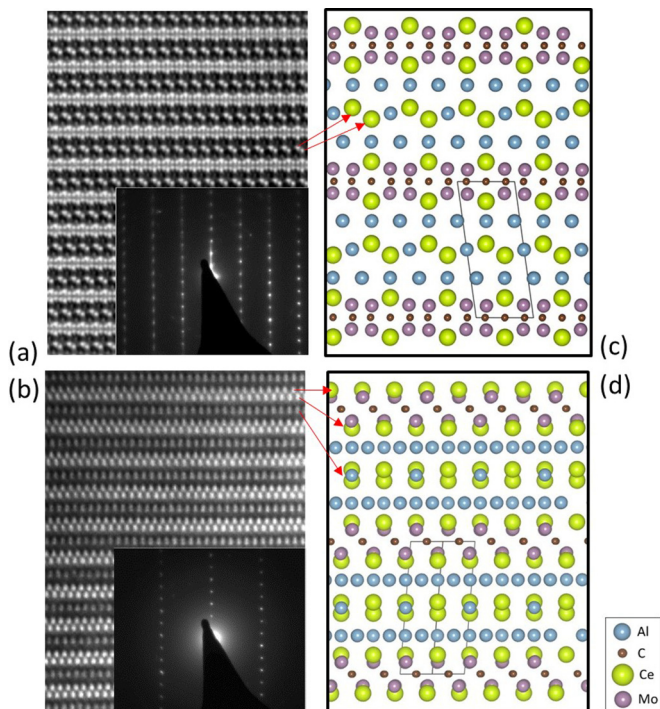

FIG. 2. STEM images from single-crystal $Mo_4Ce_4Al_7C_3$ along the (a) [110] and (b) [$\bar{1}$00] zone axes, with corresponding schematics in (c) and (d) based on a space-group 2 structure. The insets in (a) and (b) show the SAED patterns.

layers in $(Mo_{2/3}Sc_{1/3})_2AlC$ [see Fig. 1(d)]. In other words, $Mo_4Ce_4Al_7C_3$ can be viewed as an *i*-MAX phase where the Al layers are replaced by a stack of (i) one Al layer with the same kagomé lattice as in an *i*-MAX phase [see Fig. 1(c)], (ii) one Ce-Al plane defined in Fig. 1(e), and (iii) a second kagomé-like Al plane simply shifted with respect to the first one. The shift of the latter is due to the introduction of the Ce-Al plane [see Fig. 1(b)] and results in the triclinic symmetry.

We also synthesized $Mo_4Pr_4Al_7C_3$ both as powder and single crystal, and found it to be triclinic, with the same structure as $Mo_4Ce_4Al_7C_3$. Figure 3 shows STEM images of $Mo_4Pr_4Al_7C_3$ along the [110] and [$\bar{1}$00] zone axes, with corresponding schematics, obtained from a powder sample.

In the powder samples of both RE phases, we also identified an orthorhombic polymorph (space group 20, $C222_1$) with two formula units per unit cell, see Fig. 4 and Table II, showing results for $Mo_4Ce_4Al_7C_3$. The differences between the two structures are in the A-layer stacking sequence along the c axis. Interestingly, the single crystals only crystallized in the triclinic structure. In contrast, the powder samples often exhibited stacking faults and locally alternating orthorhombic and triclinic sequences. XRD on the powder sample of $Mo_4Ce_4Al_7C_3$ is shown in Fig. 5(a). Apart from the two polymorphs found by STEM analysis, a $(Mo_{2/3}Ce_{1/3})_2AlC$ *i*-MAX and Mo_2C are also present. Quantification of phase content was not performed because the sample's quality was not high. Instead, a simulated pattern based on the identified space groups is included, for comparison. XRD on a powder sample of $Mo_4Pr_4Al_7C_3$ together with the simulated pattern are correspondingly shown in Fig. 5(b). Here the impurity phases are $(Mo_{2/3}Pr_{1/3})_2AlC$ *i*-MAX and Mo_2C.

B. Vibrational properties

According to the $Mo_4Ce_4Al_7C_3$ crystal structure, the 18 atoms in the primitive cell give rise to 3 acoustic modes and 51 optical modes at the Γ point of the Brillouin zone. The
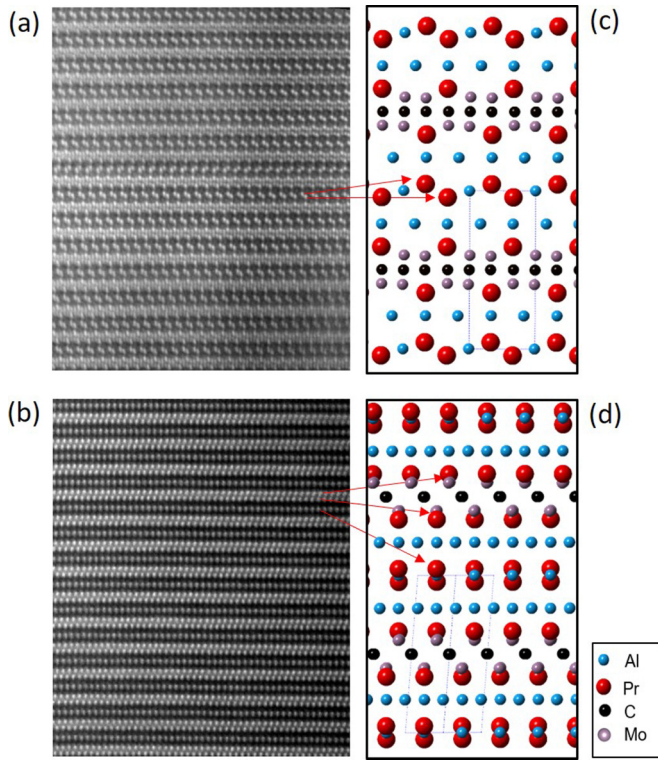
FIG. 3. STEM images from Mo$_4$Pr$_4$Al$_7$C$_3$ powder along the (a) [$\bar{1}$10] and (b) [110] zone axes, with schematics based on a space-group 2 structure.

optical-phonon modes can be classified with the following irreducible representation:

$$\Gamma_{\text{optical}} = 24A_g(\text{Raman}) + 27A_u(\text{IR}). \tag{1}$$

In Fig. 6(a) and Table III, the experimental Raman spectrum of Mo$_4$Ce$_4$Al$_7$C$_3$ is compared to the Raman-active vibrational modes predicted from the *ab initio* calculations, allowing for both a determination of the corresponding atomic structures and accurate identification of 24 Raman modes. In addition to the 24 expected lines, see Table III, four extra lines were observed in the spectra at 117, 140, and 147 cm^{-1}, with the last one, at 255 cm^{-1}, overlapping more or less with the line at 257 cm^{-1}. These additional lines suggest the existence of local structural disorder.

Based on our visualization of the vibrational modes, see Fig. 6(b), we conclude that (i) the low-frequency modes ($<$220 cm^{-1}) correspond to Ce and Mo vibrations, (ii) the Al vibrations are located in the midfrequency range ($>$220 cm^{-1}), and (iii) the high-frequency modes ($>$500 cm^{-1}) mainly involve the C and Mo atoms. This is congruent with the inverse proportionality between the vibrational frequency and the atomic mass, reported previously for other MAX phases [22].

C. Magnetization measurements

The temperature dependence of the magnetization (M) below 20 K, under a field of 1000 Oe applied parallel to the c axis, shows a steep increase at 10.5 K (inflection point) followed by a gradual saturation into a plateau down to 2 K
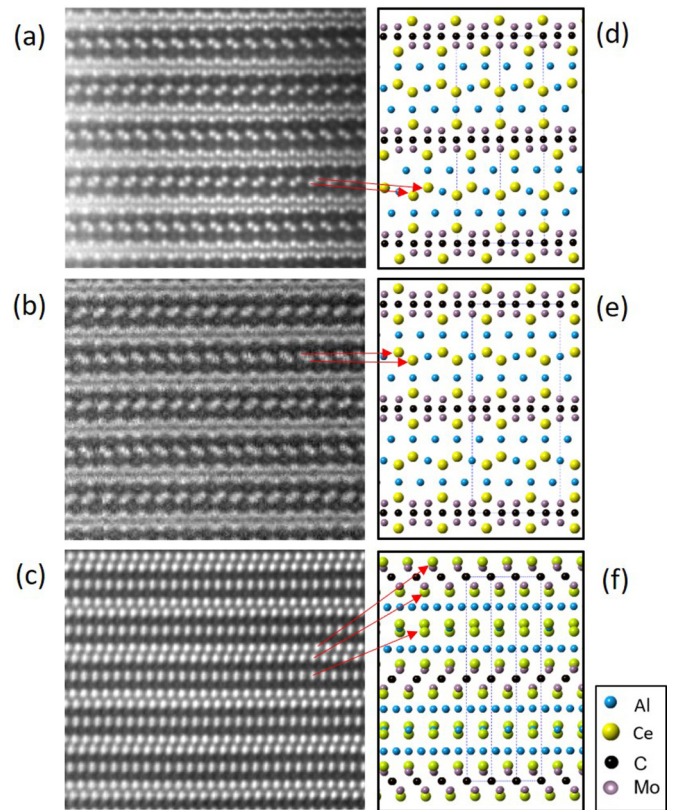

FIG. 4. STEM image of a Mo$_4$Ce$_4$Al$_7$C$_3$ polymorph, only found in the powder sample, viewed along the (a) [$\bar{1}$10], (b) [010], and (c) [100] zone axes, with corresponding schematics in (d), (e), and (f) based on a space-group 20 structure.

(Fig. 7). Similar behavior is observed when H is perpendicular to c, though with a signal that is more than ten times smaller (circles in Fig. 7). Below 7 K, a small hysteresis is observed

TABLE II. Structural parameters obtained from XRD of Mo$_4$Ce$_4$Al$_7$C$_3$ powder sample. This polymorph was only found in the powder samples.

Chemical formula	Mo$_4$Ce$_4$Al$_7$C$_3$	
Formula weight	1169.13 g/mol	
Temperature	Room temperature	
Crystal system	Orthorhombic	
Space group	20 ($C222_1$)	
Unit-cell dimensions	$a = 9.7138$ Å	$\alpha = 90°$
	$b = 5.5700$ Å	$\beta = 90°$
	$c = 22.9623$ Å	$\gamma = 90°$
Z	2	
Al	8c (0.8304 0.3307 0.6474)	
	8c (0.0860 0.0771 0.6468)	
	8c (0.5835 0.0846 0.6466)	
	4b (0.0000 0.6713 0.2500)	
C	4a (0.9952 0.0000 0.0000)	
	4a (0.6657 0.0000 0.0000)	
	4a (0.3390 0.0000 0.0000)	
Ce	8c (0.8314 0.1718 0.2697)	
	8c (0.8341 0.1595 0.4261)	
Mo	8c (0.1718 0.1729 0.4561)	
	8c (0.4947 0.1709 0.4534)	
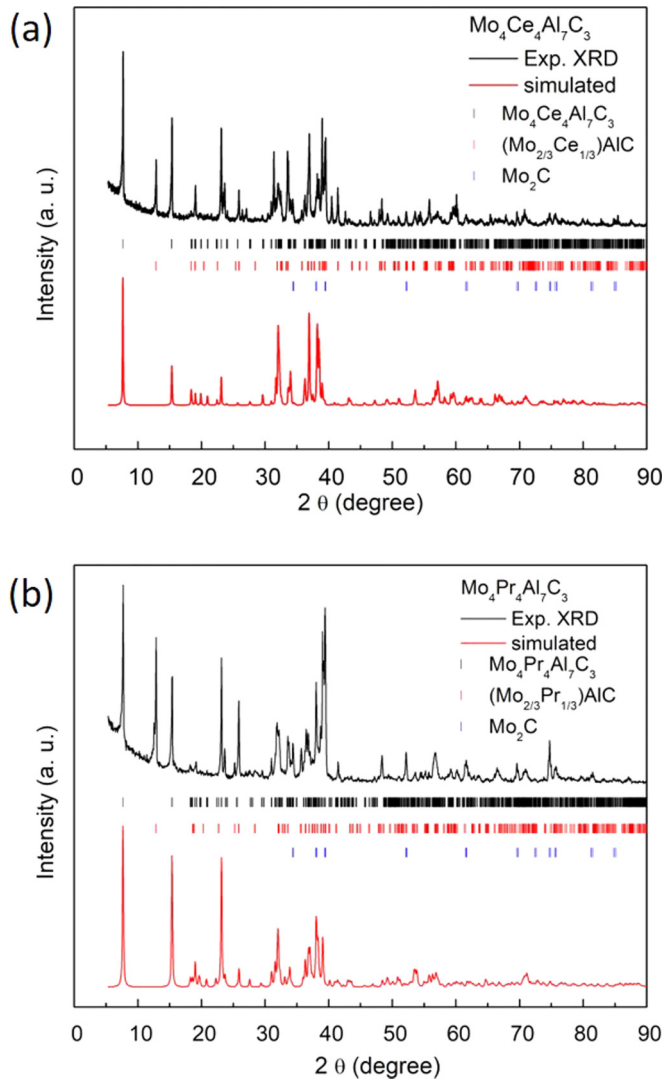
FIG. 5. XRD on powder samples of (a) $Mo_4Ce_4Al_7C_3$ and (b) $Mo_4Pr_4Al_7C_3$, with respective simulated XRD patterns from the schematic cells shown in Figs. 2 and 3. Markers below the Exp. XRD indicate the peak position of $Mo_4RE_4Al_7C_3$, *i*-MAX, and Mo_2C.

FIG. 6. (a) Typical single-crystal $Mo_4Ce_4Al_7C_3$ Raman spectrum collected at room temperature. The 24 calculated Raman-active modes are represented at the bottom of the graph, and they are classified according to the atoms involved in the vibrational modes. A representative mode of each category is presented in (b). The lengths of the black arrows are proportional to the product of the displacement and atomic mass. For the sake of clarity, not all the experimental Raman mode positions are depicted. Three additional weak lines at 117, 140, and 147 cm^{-1} are marked with stars.

between the FC and ZFC measurements. These observations are characteristic of a ferromagnetic (FM) phase transition at $T_C = 10.5$ K. More evidence for FM behavior is given by the M versus H curves shown in Figs. 8(a) and 8(b), which were obtained with H perpendicular and parallel, respectively, to the c axis. The curves reveal a large anisotropy. When H is perpendicular to c, a large hysteresis is observed with coercivity H$c = 0.23$ T. When H is parallel to c, a large magnetization with small hysteresis is observed, with H$c = 0.03$ T. These results confirm that the easy magnetization axis is along the c axis. The origin of the anisotropy is not clear at this stage.

In the paramagnetic state, above 20 K, the inverse susceptibility (χ) deduced from the Arrott plot is presented in Fig. 9 (the larger uncertainty at higher temperatures reflects the weak M signal obtained in the small single-crystal sample used). In agreement with the Curie-Weiss law, $1/\chi$ varies linearly as $1/\chi = (T - \theta_p)/C_{th}$, where θ_p is the paramagnetic Curie temperature and C_{th} is the theoretical Curie constant. Inter-estingly, the 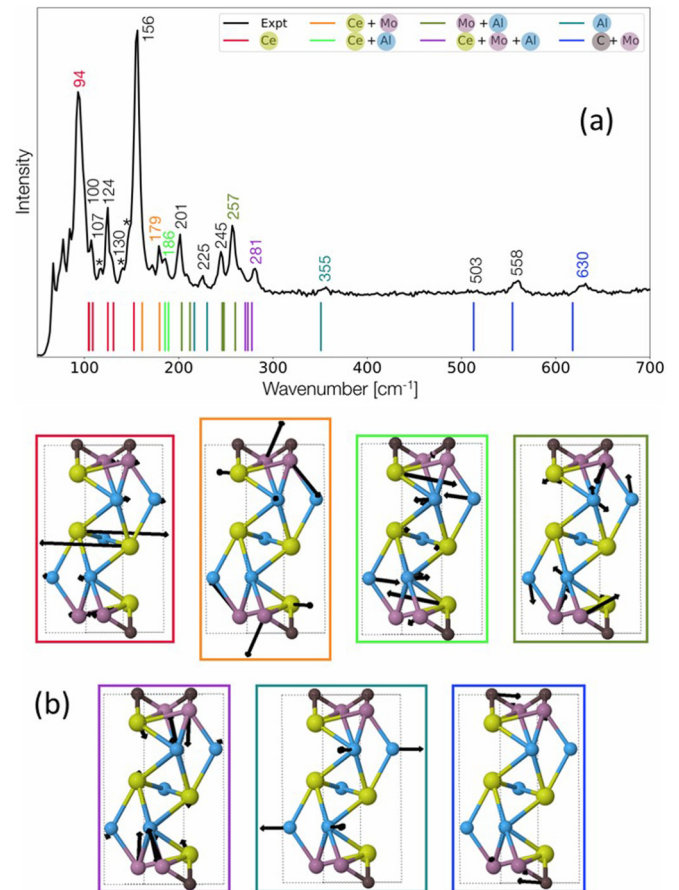slope is inconsistent with the Curie constant for Ce^{3+} ions (blue line, Fig. 9). At $2.18(8)\mu_B$, the effective moment of the Ce^{3+} ions—deduced from a linear fit of the dashed line in Fig. 9—is lower than the saturation moment expected from isolated Ce^{3+} ions in the $4f^1$ configuration, viz. $2.54\mu_B$. The dashed line shown in Fig. 9 that assumes a magnetic moment of 80 ± 3 % is clearly a much better fit to the results. We thus conclude that only $\approx 80 \pm 3$ % of the Ce ions are in a +3 valence state. This conclusion is consistent with the results obtained by XANES discussed in the next section.

It should be noted that the presence of two Ce sites, with quite different coordination, could result in Ce sites with a +3 valence and Ce sites with a mixed valence +$(4-\delta)$, in line with observations made for other compounds; see, e.g., [23]. Assuming a valence of +3 for one site, and using our magnetization data, one would expect a mixed valence of +3.28 for the other site. This value is comparable to the value of +3.36 obtained for 50% of the Ce sites—with longer bond lengths—in CeRuSn [23]. To appreciate the plausibility

TABLE III. Experimentally observed (ω_{expt}) and calculated (ω_{calc}) Raman modes in $Mo_4Ce_4Al_7C_3$. Asterisks denote additional lines.

$\omega_{\text{expt}}(\text{cm}^{-1})$	$\omega_{\text{calc}}(\text{cm}^{-1})$
94	104.5
100	105.0
107	108.9
117*	
124	124.9
130	130.8
140*	
147*	
156	152.5
172	161.2
179	179.6
186	185.5
188	189.1
201	203.2
209	212.0
211	216.6
225	230.2
239	246.2
245	248.0
255*	
257	260.0
265	270.6
268	273.3
281	277.6
355	350.9
503	512.9
558	554.1
630	617.9

of this interpretation, the coordination of the Ce1 and Ce2 ions is illustrated in Figs. 10(a) and 10(b), respectively. Empirically, the bond strength between two atoms is inversely proportional to the distance between them. Therefore, we evaluate the interatomic (ionic) distance between the two Ce
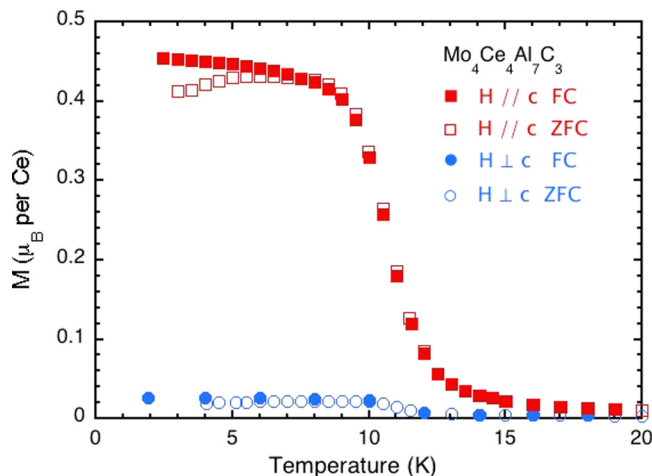

FIG. 7. Temperature dependence of the magnetization M for a $Mo_4Ce_4Al_7C_3$ single crystal under 0.1 T (FC and ZFC conditions) when H is parallel and perpendicular to c. A clear FM transition can be seen at 10.5 K.

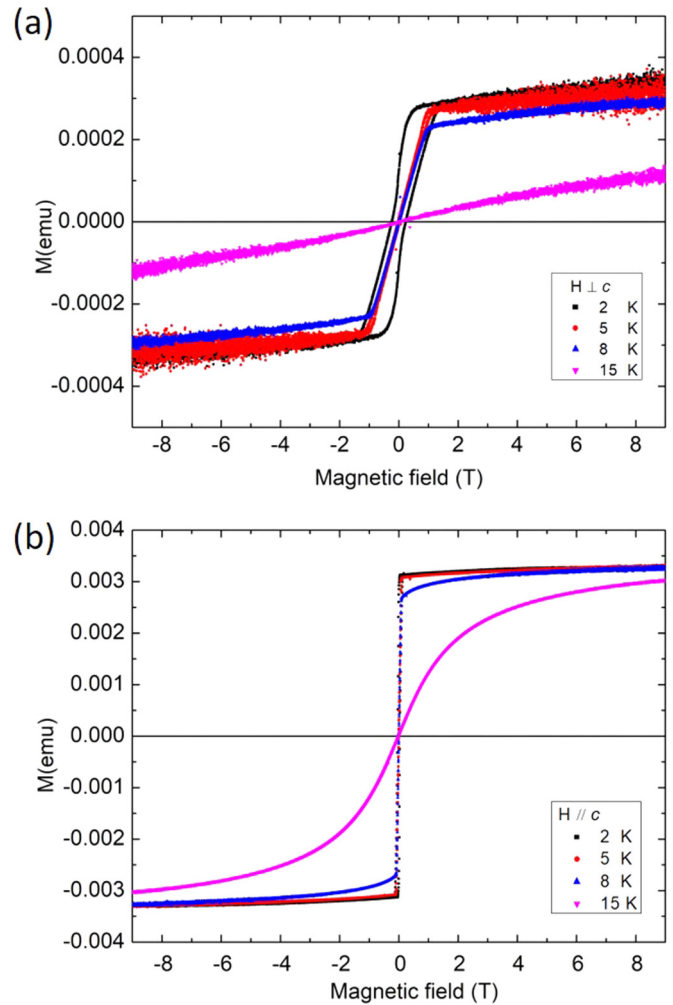FIG. 8. Isothermal M(H) curves with (a) H perpendicular to c, and (b) H parallel to the c axis. When H is perpendicular to c, a large hysteresis is observed with coercivity Hc = 0.23 T. When H is parallel to c, a large magnetization with small hysteresis is observed, with Hc = 0.03 T.

sites and their nearest atom neighbors. We define the empirical bond strength ratio as the interatomic distance divided by the sum of the covalent radii of Ce and the bonding atoms. In Fig. 10(c) we show the Ce1 sites and the bonding atoms with an empirical bond strength ratio smaller than 1.11. As can be seen, the Ce1 sites are closely bonded to Mo and C, and to a smaller extent to Ce2 ions. The same procedure is applied to the Ce2 atoms, as shown in Fig. 10(d). It appears that the Ce2 atoms are only strongly bonded to Ce1.

It is thus reasonable to conclude that the Ce1 ions are more strongly bonded to Mo and C. In the MAX phases, it is well established that the d orbitals of the M atoms dominate at the Fermi level, see, e.g., Ref. [24], where the orbital nature of the Fermi level electrons is not only predicted, but also determined from angle-resolved photoemission spectroscopy (ARPES) measurements. We thus expect a stronger hybridization of the Ce1 atoms with the itinerant Mo atoms' d states, compared with Ce2. Such a mechanism is known to induce mixed valences in a number of compounds [25]. In our case, we have no definitive clue for assigning the mixed valence
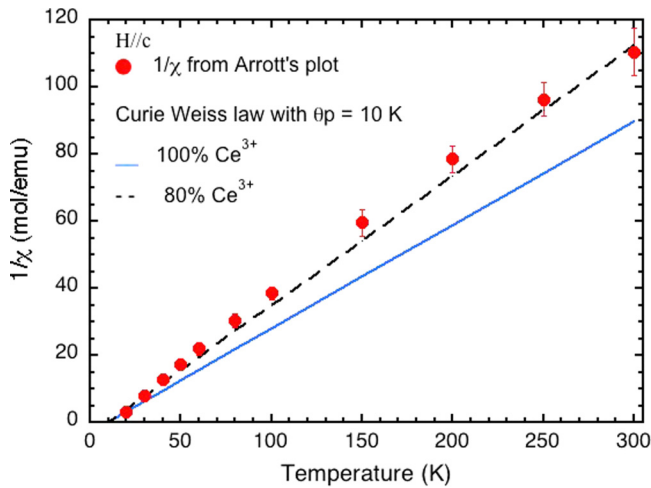
FIG. 9. Inverse magnetic susceptibility (deduced from the Arrott's plots) with H//c. The blue line represents the Curie-Weiss law curve obtained assuming 100% Ce^{3+} ions, and the black dashed line assumes 80% Ce^{3+} ions.

state to either of the two different sites. But, as discussed below, assuming that only one of the sites exhibits a mixed valence permits us to elaborate a consistent interpretation of the combined magnetization, XANES, and XMCD data.

The spontaneous M value deduced from Arrott's plot at 4 K (H//c, graph not shown) gives $0.67\mu_B$ per Ce ion. In this case, the spontaneous magnetic moment should reach $0.77\mu_B$ per Ce atom at 0 K. This value is appreciably lower than the maximum value of $2.14\mu_B$ expected at 0 K for the Ce^{3+} ion. Part of this reduction could be ascribed to the crystalline electric field that partly lifts the degeneracy of the fundamental

multiplet. However, and as reinforced by our interpretation of the XANES and XMCD data expounded in the next section, we suspect that only the Ce sites corresponding to a pure valence of +3 and $4f^1$ configuration are ferromagnetic, whereas the Ce atoms with a mixed valence of the second site and $4f^1$ configuration are paramagnetic. In this scheme, only half of the Ce atoms (those of the site with a pure $4f^1$ configuration) would contribute to the spontaneous moment, giving $1.54\mu_B$, a more reasonable value, for Ce^{3+} ions.

D. XANES and XMCD

In the ground state of mixed valence Ce compounds, the energies of the Ce $4f^0$ (tetravalent Ce^{4+}) and $4f^1$ (trivalent Ce^{3+}) configurations are close to each other and mixed by the hybridization between the $4f$ electrons and the $5d$ conduction-band states. In the final state of the Ce L_3 XANES, however, the energies of the two configurations are separated by a strong core-hole potential (of the order of 10 eV) acting on the $4f$ state, so that the XANES spectrum exhibits two peaks. This is usually taken as evidence of the mixed valence state [26–29]. Analyzing the intensity ratios of the two peaks, we were able to estimate the average valence state of the Ce ions and the average Ce $4f$ magnetic moment was quantitatively determined from the XMCD results (see below).

The XANES spectra recorded at the Ce $L_{3,2}$ edges of $Mo_4Ce_4Al_7C_3$ are shown in Fig. 11 (left axis). The spectra are dominated by the electric dipolar transitions ($2p \rightarrow 5d$). The main resonances ("white lines") at the L_3 and L_2 absorption edges show a clear double peak structure, which as just noted is commonly identified as the signature of a mixed valence ground state [26–29]. The low-energy peak at ~5726 eV is related to the $4f^1$ configuration, whereas the high-energy
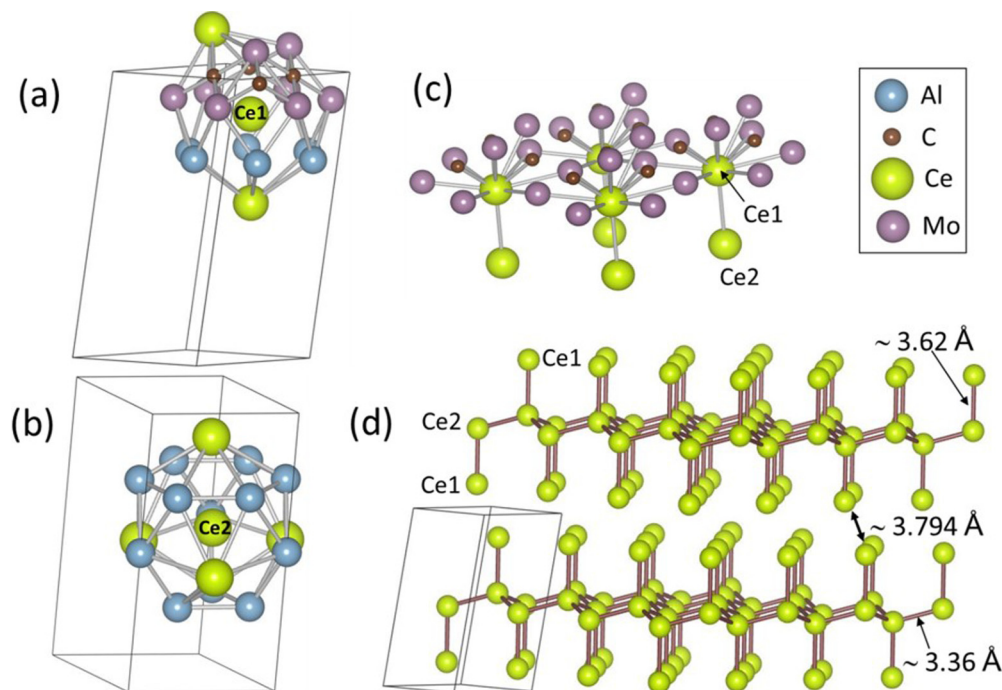

FIG. 10. Coordination of Ce1 and Ce2 atom sites. (a) Ce1 atom surrounded by its nearest neighbors. (b) Ce2 atom surrounded by its nearest neighbors. (c) A schematic of the Ce1 atom plane and the bonding atoms with an empirical bond strength ratio smaller than 1.11. (d) A schematic obtained using the same procedure as for (c), but applied to the Ce2 atoms.
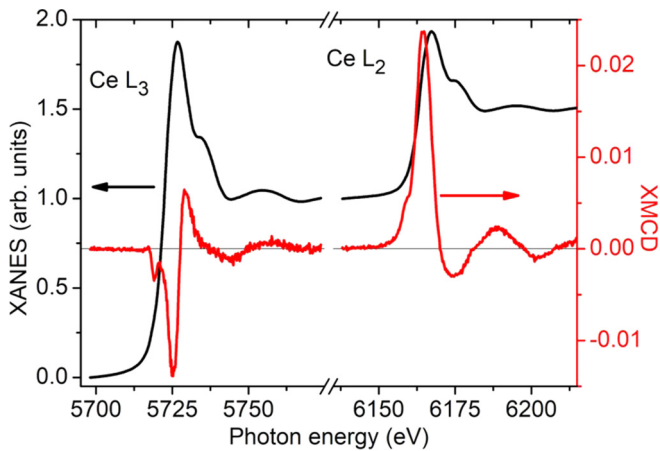
FIG. 11. Normalized XANES (left axis) and XMCD (right axis) spectra measured at the Ce $L_{3,2}$ edges on a $Mo_4Ce_4Al_7C_3$ crystal at $T = 2.1$ K and $H = 1$ T. The spectra have been corrected for self-absorption effects and circular polarization rate.

peak is assigned to transitions within the $4f^{\circ}$ configuration in the ground state of the Ce ions. A quantification of the electronic states can be obtained by estimating the relative spectral weights of the $4f^1$ and $4f^{\circ}$ features. A fitting procedure [30]—using a sum of two Lorentzians and two arctangent curves to decompose the Ce L_3-edge XANES—generally applied for such data analysis [31] was used here for this purpose. Following this procedure (see Appendix B), we estimate that the relative weight of the $4f^0$ configuration [defined as the ratio $4f^0/(4f^0 + 4f^1)$] is $\sim 25 \pm 5\%$, which corresponds to an average Ce $4f$ electron count of 0.75 ± 0.05.

Figure 12 (left axis) shows the XANES recorded at the Mo $L_{3,2}$ edges. At first glance, the spectral shape of the white line at the Mo L_3 edge is mostly composed of a single, broad peak located at 2522 eV. However, one can notice a weak shoulder located at higher energy (~ 2526 eV), reflecting crystal-field splitting [32]. The overall white lines at the Mo $L_{3,2}$ edges are rather broad and point out the delocalized character of
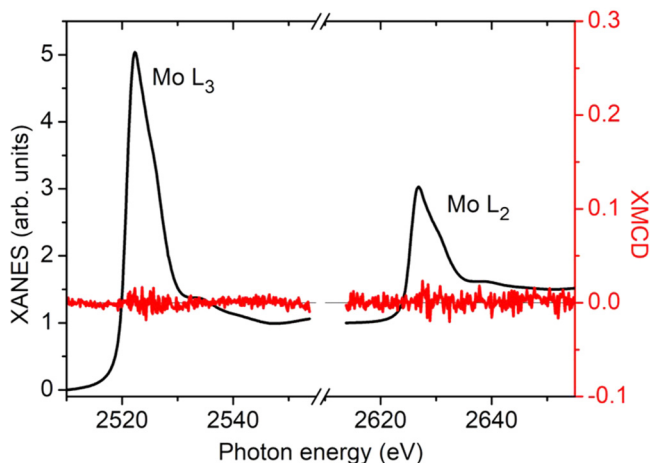

FIG. 12. Normalized XANES (left axis) and XMCD (right axis) spectra measured at the Mo $L_{3,2}$ edges in a $Mo_4Ce_4Al_7C_3$ crystal at $T = 2.1$ K and $H = 1$ T. Spectra have been corrected for self-absorption effects and circular polarization rates.
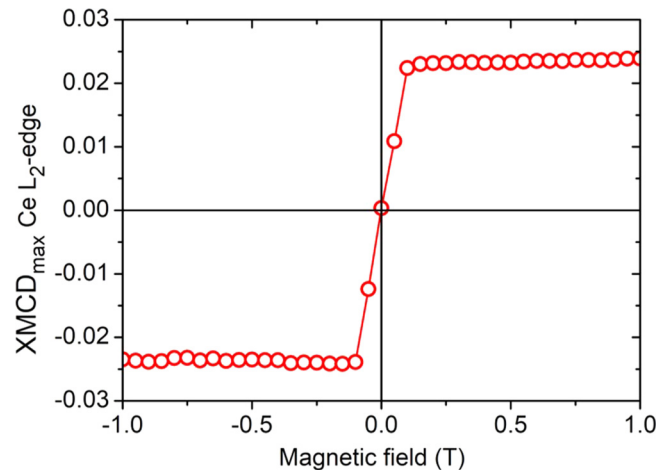

FIG. 13. Element-specific XMCD intensity vs H measured at the Ce L_2 edge at $E = 6164.5$ eV at $T = 2.1$ K. A typical ferromagnetic behavior is observed, confirming the FM ordering of Ce $4f$ moments.

the Mo $4d$ electrons. This agrees with the predictions and experimental verifications made for previously studied MAX phases; see, e.g., Ref. [24].

Figure 11 (right axis) shows the XMCD spectra recorded at the Ce $L_{3,2}$ edges at 2.1 K under a 1 T magnetic field. The existence of a finite XMCD signal at both L_3 and L_2 edges confirms that the Ce ions are carrying a magnetic moment. The spectral shape of the XMCD signals is characteristic of a $4f^1$ system, as observed in $CeRu_2Ge_2$ [33] or CeH_2/Fe multilayers [34], and consequently demonstrates that the Ce atoms are the main source of magnetism in $Mo_4Ce_4Al_7C_3$. The magnetic field dependence of the maximum dichroic signal at the Ce L_2 edge (Fig. 13) confirms ferromagnetic ordering of the Ce $4f$ moments. It should be stressed that the observation of only one magnetic peak corresponding to the main $4f^1$ final state demonstrates that only this channel leads to ferromagnetism. In contrast, the Ce ions with a mixed valent state exhibit a double-peak XMCD spectrum as observed in highly hybridized Ce systems with $3d$/$4d$ ions, e.g., $Ce(Pd_{1-x}Ni_x)_3$ [35]. In our case, such a double-peak XMCD signal is not observed at the Ce L_3 edge, meaning that the Ce ions with a mixed valent state are not involved in the ferromagnetism.

The above interpretation is also supported by the observation of a rather strong XMCD signal at the electric quadrupolar transitions ($2p \rightarrow 4f$) located ~ 7 eV below the first XANES peak (Fig. 11). Even at the L_2 edge of Ce, those transitions are clearly observable as a shoulder in the XMCD signal. We can therefore propose a model in which two nonequivalent Ce sites are contributing differently to the magnetic properties. One site is occupied by Ce ions with localized $4f$ states featuring a $4f^1$ configuration and is responsible for ferromagnetism. Since Ce ions in $CeAl_2$ [36] and $CeAl_3$ are known to be $4f^1$, we tentatively suggest that it is the Ce atoms in Ce2 sites that are ferromagnetically coupled. The $4f$ states of the Ce1 site seem to be strongly delocalized and exhibit mixed valence behavior with Pauli-type paramagnetic response as observed in $Ce(Pd_{1-x}Ni_x)_3$ [35]. Our XMCD measurements were performed under a magnetic field of only

1 T, and this prevented us from observing double-peak XMCD from the latter site. Finally, we estimate the magnetic moment carried by Ce $4f$ electrons on a Ce2 site by comparing the experimental XMCD signals (see Fig. 11) with those recorded from the CeRu$_2$Si$_2$ ferromagnet carrying $\sim$1.5μ_B at magnetic saturation [37]. In the present case, the XMCD signal per Ce ion is about 2.6 times weaker, i.e., about 0.6μ_B, which is in good agreement with our macroscopic magnetization measurements. However, if we consider that only atoms on the Ce2 site in carry a magnetic moment, it is approximately 1.2μ_B.

We also attempted to measure the magnetic properties of Mo atoms. Indeed, within the detection level of our measurements, no distinguishable XMCD signal was observed at the Mo $L_{3,2}$ edges (noisy horizontal red line in Fig. 12), confirming that the Ce in the Ce1 site is paramagnetic. Based on previous XMCD measurements performed at the $L_{3,2}$ edges of Mo [38,39], the Mo $4d$ magnetic moment induced by Ce, if any, should be lower than 0.01μ_B.

E. Electronic structure

Many of the MAX phases are characterized by a quasi-2D electronic band structure [40]. For example, a recent ARPES study on Cr$_2$AlC reveals an open, tubular electron and hole band structure along the c axis [24]. As discussed above, Mo$_4$Ce$_4$Al$_7$C$_3$ and Mo$_4$Pr$_4$Al$_7$C$_3$ can be regarded as i-MAX phases with three A layers. Similar to the i-MAX [41] or MAX phases [9], the electronic states near the Fermi level are likely dominated by the M d electrons. Since the additional A layers substantially increase the interlayer spacing between the M layers, it would be interesting to verify if this enhances the quasi-2D character of these RE-based phases. In addition, the strongly correlated Ce $4f$ electrons and their probable hybridization with Mo $4d$ electrons may make the

electronic structure intriguing [42,43]. ARPES measurements on Mo$_4$Ce$_4$Al$_7$C$_3$ single crystals are in progress.

IV. CONCLUSIONS

Herein we report on a family of layered RE compounds with a Mo$_4$RE$_4$Al$_7$C$_3$ chemistry, where RE = Ce and Pr. While powder samples of both phases crystallized in two polymorphs—triclinic (space group 2) and orthorhombic (space group 20)—the single-crystal samples crystallized solely in the triclinic structure. These 4473 phases are comprised of i-MAX blocks—viz. (Mo$_{2/3}$RE$_{1/3}$)$_2$C layers wherein the Mo and RE atoms are ordered—interleaved with three A layers comprised of Al and Ce atoms only.

The observed Raman modes of Mo$_4$Ce$_4$Al$_7$C$_3$ were in good agreement with DFT calculations. As for the MAX phases, the higher-energy modes are dominated by the C atoms occupying the octahedral sites between the Mo and Ce sites. Furthermore, below $\sim$10 K, the ground state is ferromagnetic. We also provide strong arguments based on x-ray spectroscopy that the two nonequivalent Ce sites exhibit different electronic and magnetic properties. The Ce2 site features localized $4f^1$ states with ferromagnetically ordered $4f$ moments of about 1.2μ_B, whereas the Ce1 site occupied by ions with strongly delocalized $4f$ electrons are not involved with the ferromagnetism.

The discovery of any new layered magnetic material is noteworthy. However, since at this time there is no reason to believe that this family is restricted to Ce and Pr, and other RE elements—and quite possibly non-RE elements—this discovery is potentially quite important. The prospect of converting these 3D solids to their 2D analogs or MXenes is also quite exciting. We have recently shown that it is possible to etch both the Al and Sc atoms from the i-MAX phase (Mo$_{2/3}$Sc$_{1/3}$)$_2$AlC. The fact that the A layers present between

TABLE IV. Data collection and structure refinement for the Mo$_4$Ce$_4$Al$_7$C$_3$ single crystals.

Theta range for data collection	3.53°–36.45°
Index ranges	$-9 \Leftarrow h \Leftarrow 9,\ -9 \Leftarrow k \Leftarrow 9,\ -19 \Leftarrow l \Leftarrow 19$
Reflections collected	57 227
Independent reflections	3037[R(int) = 0.0342]
Absorption correction	Numerical Mu from Formula
Max. and min. transmission	0.6130 and 0.0620
Structure solution technique	direct methods
Structure solution program	XT, VERSION 2014/5
Refinement method	Full-matrix least-squares on F^2
Refinement program	SHELXL-2014/7 [44]
Function minimized	$\Sigma\, w(F_o^2 - F_c^2)^2$
Data / restraints / parameters	3037 / 0 / 80
Goodness-of-fit on F^2	1.294
Final R indices	3012 data; $I > 2\sigma(I) R1 = 0.0205,\ wR2 = 0.0460$
	all data $R1 = 0.0207,\ wR2 = 0.0461$
Weighting scheme	$w = 1/[\sigma^2(F_o^2) + (0.0079P)^2 + 3.5381P]$
	Where $P = (F_o^2 + 2F_c^2)/3$
Extinction coefficient	0.0005(1)
Largest diff. peak and hole	3.331 and $-2.336\,e\text{Å}^{-3}$
rms deviation from mean	0.304 $e\text{Å}^{-3}$

TABLE V. Anisotropic atomic displacement parameters obtained from structure refinement of Mo$_4$Ce$_4$Al$_7$C$_3$ single crystals. The anisotropic atomic displacement factor exponent takes the form $-2\pi^2[h^2 a^{*2} U_{11} + \; + 2hk\, a^* b^* U_{12}]$.

	U_{11}	U_{22}	U_{33}	U_{23}	U_{13}	U_{12}
Ce1	0.00119(6)	0.00088(6)	0.00253(6)	−0.00024(4)	−0.00007(4)	−0.00042(5)
Ce2	0.00495(7)	0.00435(7)	0.00414(7)	−0.00041(5)	0.00003(5)	−0.00216(5)
Mo1	0.00156(9)	0.00104(9)	0.00291(9)	−0.00017(7)	−0.00006(7)	−0.00054(7)
Mo2	0.00154(9)	0.00114(9)	0.00253(9)	−0.00045(7)	0.00013(7)	−0.00054(7)
Al1	0.0030(4)	0.0029(4)	0.0040(4)	−0.0005(3)	0.0000(3)	−0.0011(3)
Al2	0.0038(5)	0.0027(5)	0.0088(6)	−0.0011(4)	0.0000(4)	−0.0016(4)
Al3	0.0036(4)	0.0032(4)	0.0042(4)	−0.0006(3)	0.0000(3)	−0.0019(3)
Al4	0.0034(4)	0.0027(4)	0.0040(4)	−0.0005(3)	−0.0001(3)	−0.0013(3)
C1	0.0017(8)	0.0017(8)	0.0046(8)	−0.0006(7)	0.0001(7)	−0.0009(6)
C2	0.0017(8)	0.0017(8)	0.0046(8)	−0.0006(7)	0.0001(7)	−0.0009(6)

the MX blocks are Al-rich bodes well for converting them to their 2D counterparts.

APPENDIX A: STRUCTURE DETERMINATION DETAILS

The integration of the data using a triclinic unit cell yielded a total of 57 227 reflections to a maximum θ angle of 36.45° (0.60 Å resolution), of which 3037 were independent (average redundancy 18.843, completeness = 99.8%, $R_{\text{int}} = 3.42\%$, $R_{\text{sig}} = 1.12\%$) and 3012 (99.18%) were greater than $2\sigma(F^2)$. Refinement leads to the final cell constants given in Table I. The ratio of minimum to maximum apparent transmission was 0.098. The calculated minimum and maximum transmission coefficients (based on crystal size) were 0.0620 and 0.6130. The structure was solved and refined with SHELXTL, using the space group $P-1$, with $Z = 1$ for the formula unit Mo$_4$Ce$_4$Al$_7$C$_3$. The final anisotropic full-matrix least-squares refinement on F^2 with 80 variables converged at $R1 = 2.05\%$ for the observed data and $wR2 = 4.61\%$ for all

data. The goodness-of-fit was 1.294. The largest peak in the final difference electron density synthesis was $3.331\,e^-/\text{Å}^3$ and the largest hole was $-2.336\,e^-/\text{Å}^3$ with a rms deviation of $0.304\,e^-/\text{Å}^3$. On the basis of the final model, the calculated density was 6.252 g/cm^3 and $F(000)$, 509e^-. Details of the data collection and structure refinement are summarized in Table IV. Anisotropic atomic displacement parameters are summarized in Table V. Further information on crystal structure refinement is given in the cif files, which may be obtained from the Cambridge Crystallographic Data Centre, on quoting the depository numbers CCDC 1854775.

APPENDIX B: DECONVOLUTION OF THE XANES SPECTRA

For the determination of the valence state of the Ce atoms, we used a deconvolution technique proposed many years ago for intermetallic Ce compounds [30] (see Fig. 14). It assumes that the L_3 absorption spectrum of either a Ce^{3+} or a Ce^{4+} atom could be represented by a sum of an arctangent function describing transitions from the $2p$ core state into continuum and a Lorentzian function accounting for transitions into an unoccupied $5d$ band of Ce. To fit the experimental spectrum, we used the same width of the Lorentzians and
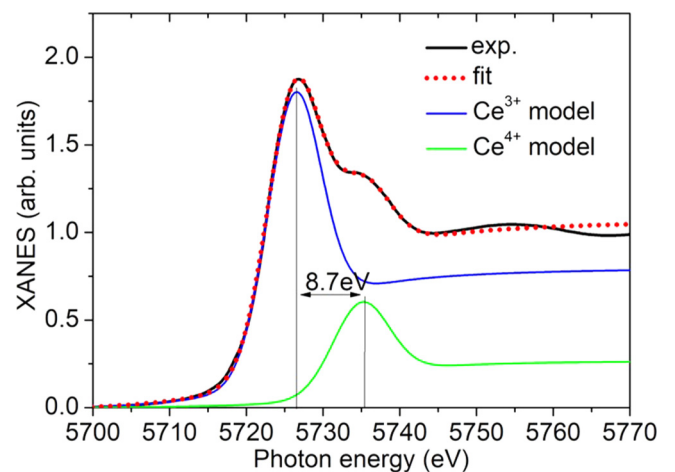

FIG. 14. Deconvolution of the experimental Ce L_3-edge XANES spectrum into a sum of model spectra for Ce^{3+} and Ce^{4+} atoms using the procedure described in Appendix B.

arctangent functions for both Ce valence states. The value of ≈ 3.5 eV is determined by the core-hole lifetime [45]. The sum of the model spectra is normalized to unity. The energy positions of the Lorentzian maxima were chosen to coincide

with the inflection points of the corresponding arctangent functions. The only two fitting parameters were the difference in energy between the two arctangent functions and the relative weight of the Ce atoms with the given valence state.

[1] P. S. Riseborough, Adv. Phys. **49**, 257 (2000).

[2] M. Dzero, J. Xia, V. Galitski, and P. Coleman, Annu. Rev. Condens. Matter Phys. **7**, 249 (2016).

[3] Y. Xu, C. Yue, H. Weng, and X. Dai, Physical Review X **7**, 011027 (2017).

[4] M. Brando, D. Belitz, F. M. Grosche, and T. Kirkpatrick, Rev. Mod. Phys. **88**, 025006 (2016).

[5] S. Wirth and F. Steglich, Nat. Rev. Mater. **1**, 16051 (2016).

[6] M. Sundermann, H. Yavaş, K. Chen, D.J. Kim, Z. Fisk, D. Kasinathan, M. W. Haverkort, P. Thalmeier, A. Severing, and L. H. Tjeng, Phys. Rev. Lett. **120**, 016402 (2018).

[7] L. Daukiya, M. N. Nair, S. Hajjar-Garreau, F. Vonau, D. Aubel, J. L. Bubendorff, M. Cranney, E. Denys, A. Florentin, G. Reiter, and L. Simon, Phys. Rev. B **97**, 035309 (2018).

[8] M. Naguib, M. Kurtoglu, V. Presser, J. Lu, J. Niu, M. Heon, L. Hultman, Y. Gogotsi, and M. W. Barsoum, Adv. Mater. **23**, 4248 (2011).

[9] M. W. Barsoum, *MAX Phases: Properties of Machinable Ternary Carbides and Nitrides* (Wiley, Weinheim, 2013).

[10] Q. Tao, M. Dahlqvist, J. Lu, S. Kota, R. Meshkian, J. Halim, J. Palisaitis, L. Hultman, M. W. Barsoum, P. O.Å. Persson, and J. Rosen, Nat. Commun. **8**, 14949 (2017).

[11] M. Dahlqvist, J. Lu, R. Meshkian, Q. Tao, L. Hultman, and J. Rosen, Sci. Adv. **3**, e1700642 (2017).

[12] R. Meshkian, M. Dahlqvist, J. Lu, B. Wickman, J. Halim, J. Thörnberg, Q. Tao, S. Li, S. Intikhab, J. Snyder, M. W. Barsoum, M. Yildizhan, J. Palisaitis, L. Hultman, P. O. Å. Persson, and J. Rosen, Adv. Mater. **30**, 1706409 (2018).

[13] I. Persson, A. Ghazaly, Q. Tao, J. Halim, S. Kota, V. Darakchieva, J. Palisaitis, M. W. Barsoum, J. Rosen, and P. O. Å. Persson, Small **14**, 1703676 (2018).

[14] Q. Tao (unpublished).

[15] T. Ouisse, E. Sarigiannidou, O. Chaix-Pluchery, H. Roussel, B. Doisneau, and D. Chaussende, J. Cryst. Growth **384**, 88 (2013).

[16] L. Shi, T. Ouisse, E. Sarigiannidou, O. Chaix-Pluchery, H. Roussel, D. Chaussende, and B. Hackens, Acta Mater. **83**, 304 (2015).

[17] G. M. Sheldrick, Acta Crystallogr., Sect. C **71**, 3 (2015).

[18] X. Gonze, B. Amadon, P. M. Anglade, J. M. Beuken, F. Bottin, P. Boulanger, F. Bruneval, D. Caliste, R. Caracas, M. Côté, T. Deutsch, L. Genovese, Ph. Ghosez, M. Giantomassi, S. Goedecker, D. R. Hamann, P. Hermet, F. Jollet, G. Jomard, S. Leroux, M. Mancini, S. Mazevet, M. J. T. Oliveira, G. Onida, Y. Pouillon, T. Rangel, G. M. Rignanese, D. Sangalli, R. Shaltaf, M. Torrent, M. J. Verstraete, G. Zerah, and J. W. Zwanziger, Comput. Phys. Commun. **180**, 2582 (2009).

[19] J. P. Perdew, K. Burke, and M. Ernzerhof, Phys. Rev. Lett. **77**, 3865 (1996).

[20] D. R. Hamann, Phys. Rev. B **88**, 085117 (2013).

[21] A. Rogalev and F. Wilhelm, Phys. Met. Metallogr. **116**, 1285 (2015).

[22] N. J. Lane, M. Naguib, V. Presser, G. Hug, L. Hultman, and M. W. Barsoum, J. Raman Spectroscopy **43**, 954 (2012).

[23] R. Feyerherm, E. Dudzik, S. Valencia, J. A. Mydosh, Y.-K. Huang, W. Hermes, and R. Pöttgen, Phys. Rev. B **85**, 085120 (2012).

[24] T. Ito, D. Pinek, T. Fujita, M. Nakatake, S.-i. Ideta, K. Tanaka, and T. Ouisse, Phys. Rev. B **96**, 195168 (2017).

[25] A. Fujimori, Phys. Rev. B **28**, 4489 (1983).

[26] J. Röhler, in *X-ray Absorption and Emission Spectra*, edited by K. A. Gschneider, Jr., L. Eyring, and S. Hüfner, Handbook on Physics (North-Holland, Amsterdam, 1987), Vol. 10.

[27] D. Wohlleben and J. Röhler, J. Appl. Phys. **55**, 1904 (1984).

[28] J.-C. Parlebas, K. Asakura, A. Fujiwara, I. Harada, and A. Kotani, Phys. Rep. **431**, 1 (2006).

[29] A. Kotani, K. O. Kvashnina, P. Glatzel, J. C. Parlebas, and G. Schmerber, Phys. Rev. Lett. **108**, 036403 (2012).

[30] J. Röhler, J. Magn. Magn. Mater. **47**, 175 (1985).

[31] O. Isnard, S. Miraglia, D. Fruchart, C. Giorgetti, S. Pizzini, E. Dartyge, G. Krill, and J. P. Kappler, Phys. Rev. B **49**, 15692 (1994).

[32] F. De Groot, Z. Hu, M. Lopez, G. Kaindl, F. Guillot, and M. Tronc, J. Chem. Phys. **101**, 6570 (1994).

[33] W. Grange, J.-P. Kappler, E. Dartyge, P. Haen, P. Lejay, and A. Rogalev, Phys. B **259**, 1142 (1999).

[34] M. Arend, M. Finazzi, O. Schutte, M. Münzenberg, A.-M. Dias, F. Baudelet, Ch. Giorgetti, E. Dartyge, P. Schaaf, J.-P. Kappler, G. Krill, and W. Felsch, Phys. Rev. B **57**, 2174 (1998).

[35] J.-P. Kappler, A. Herr, G. Schmerber, A. Derory, J.-C. Parlebas, N. Jaouen, F. Wilhelm, and A. Rogalev, Eur. Phys. J. B **37**, 163 (2004).

[36] C. Chang, C. Dong, C. Huang, and Y. Chen, J. Appl. Phys. **87**, 3349 (2000).

[37] P. Haen, J. Flouquet, F. Lapierre, P. Lejay, and G. Remenyi, J. Low Temp. Phys. **67**, 391 (1987).

[38] M. Besse, V. Cros, A. Barthélémy, H. Jaffrès, J. Vogel, F. Petroff, A. Mirone, A. Tagliaferri, P. Bencok, P. Decorse, P. Berthet, Z. Szotek, W. M. Temmerman, S. S. Dhesi, N. B. Brookes, A. Rogalev, and A. Fert, Europhys. Lett. **60**, 608 (2002).

[39] M.-A. Arrio, J. Long, C. Cartier dit Moulin, A. Bachschmidt, V. Marvaud, A. Rogalev, C. Mathoniere, F. Wilhelm, and P. Sainctavit, J. Phys. Chem. C **114**, 593 (2009).

[40] T. Ouisse and M. W. Barsoum, Mater. Res. Lett. **5**, 365 (2017).

[41] A. Thore and J. Rosén, Phys. Chem. Chem. Phys. **19**, 21595 (2017).

[42] M. Neupane, N. Alidoust, S-Y. Xu, T. Kondo, Y. Ishida, D. J. Kim, C. Liu, I. Belopolski, Y. J. Jo, T-R. Chang, H-T. Jeng, T. Durakiewicz, L. Balicas, H. Lin, A. Bansil, S. Shin, Z. Fisk, and M. Z. Hasan, Nat. Commun. **4**, 2991 (2013).

[43] E. Bauer, A. Slebarski, E. Freeman, C. Sirvent, and M. Maple, J. Phys.: Condens. Matter **13**, 4495 (2001).

[44] G. M. Sheldrick, *SHELXL-2014 Pogram for Crystal Structure Solution and Refinement* (University of Göttingen, Göttingen, Germany, 2014).

[45] M. O. Krause, J. Phys. Chem. Ref. Data **8**, 307 (1979).